RSC Advances

PAPER

View Article Online
View Journal | View Issue

Cite this: *RSC Adv.*, 2022, **12**, 22244

A hybrid composite of $H_2V_3O_8$ and graphene for aqueous lithium-ion batteries with enhanced electrochemical performance

Wenyuan Duan,[a] Yanlin Li,*[b] Yeming He,[a] Duqiang Xin,[a] Najeeb ur Rehman Lashari,[c] Cheng Ma,[a] Yuzhen Zhao*[a] and Zongcheng Miao*[d]

Received 7th July 2022
Accepted 25th July 2022

DOI: 10.1039/d2ra04196k

rsc.li/rsc-advances

Aqueous rechargeable lithium-ion batteries (ARLBs) are regarded as a competitive challenger for large-scale energy storage systems because of their high safety, modest cost, and green nature. A kind of modified composite material composed of $H_2V_3O_8$ nanorods and graphene sheets (HVO/G) has been effectively made by a one-step hydrothermal method and following calcination at 523 K. XRD, SEM, TEM, and TG are used to determine the phase structures and morphologies of the composite materials. Owing to the advantage of the layered structure of $H_2V_3O_8$ nanorods, the excellent conductivity of the graphene sheets, and the 3D network structure of the modified composite, the ARLBs with HVO/G can deliver an adequate specific capacity of 271 mA h g^{-1} at 200 mA g^{-1} and have a retention rate of 73.4% after 50 cycles. The average discharge capacity of ARLB with HVO/G as anode has a considerable improvement over that of HVO/CNTs and HVO, whatever the current rate used. Moreover, we find that the diffusion coefficient of lithium-ion increases by an order of magnitude through the theoretical calculation for HVO/G ARLB. The new ARLB with HVO/G electrode is a potential energy storage system with great advantages, such as simple preparation, easy assembly process, excellent safety and low-cost environmental protection.

Introduction

With the extensive use of fossil energy, the problem of environmental pollution is becoming increasingly severe, and the unit price of energy is gradually rising.[1,2] There have been some policies and ordinances introduced by national and international organizations to encourage green energy, including solar energy, wind energy, hydropower, and tidal energy. These energy sources are cyclical. Therefore, energy storage systems are required to balance peaks and troughs.[3] In the foreseeable future, the global demand for energy storage systems will increase tremendously.

Traditional lithium-ion batteries (LIBs) display a superior energy density, which has great utilization value in the field of energy storage devices such as electric vehicles, electronic equipment, and space equipment.[4,5] However, the future of traditional LIBs for large-scale storage has been questionable recently.[6,7] Environmental pollution is a serious problem for LIBs due to the use of organic electrolytes.[8,9] Moreover, the harsh equipment process and equipment conditions, as well as the uneven distribution of lithium elements, will lead to the higher and higher cost of LIBs in the long run.[10] There is no doubt that cost, safety, and environmental feature are crucial factors in the large-scale storage system.[11,12]

Compared to risky and expensive LIBs with organic electrolytes, aqueous rechargeable lithium-ion batteries (ARLBs) batteries with inorganic electrolytes have their advantages in the large-scale energy storage system since it was reported by Dahn in the mid-1990s.[13] Once the ARLBs were invented, they have quickly attracted much attention from researchers in many fields due to environmental friendliness, low cost, excellent safety and good ionic conductivity of the aqueous inorganic electrolyte when charging and discharging at high current density.[8] Wang reported the application of olivine $FePO_4$ as anode material for aqueous lithium-ion batteries.[14] Professor Wu's team introduced a coating layer on lithium metal in ARLB to increase the discharge voltage to 4.0 V.[15] Caballero researched the reason for the LiV_3O_8 as an ARLB electrode material has electrochemical instability.[16]

ARLBs has similar working principles to LIBs, but not all electrode materials for LIBs work well in ARLBs because of side reaction in aqueous electrolytes, such as H_2 and O_2 evolution.[8] Therefore, finding suitable electrode materials for ARLBs and improving their electrochemical performance are the main

[a]Xi'an Key Laboratory of Advanced Photo-electronics Materials and Energy Conversion Device, Xijing University, Xi'an 710123, China. E-mail: zyz19870226@163.com
[b]School of Materials Science and Engineering, Xi'an University of Architecture & Technology, Xi'an 710055, China. E-mail: liyanlin@xauat.edu.cn
[c]Institute for Advanced Study, Shenzhen University, Shenzhen, 518060, China
[d]School of Artificial Intelligence, Optics and Electronics (iOPEN), Northwestern Polytechnical University, Xi'an, 710072, China. E-mail: miaozongcheng@nwpu.edu.cn

research directions.[17] Yuan *et al.* synthesized a series of Al-doped $LiAl_xMn_{2-x}O_4$ by solid sintering.[18] Yang *et al.* reported the electrochemical properties of $LiMn_2O_4$ an aqueous solution with different pH values.[19]

In several battery systems, layered vanadium oxides have been seen as a viable rival such as LIBs and ARLBs,[20,21] which can accommodate Li^+ insertion/extraction due to the layer structure. $H_2V_3O_8$ materials were firstly reported as potential cathode materials for LIBs in 2006 and then were demonstrated as the competitive anodes for aqueous rechargeable lithium-ion batteries (ARLBs) in 2011.[22,23] $H_2V_3O_8$ (or $V_3O_7 \cdot H_2O$) is made up of VO_6 octahedra and VO_5 trigonal bipyramids, and it has a greater theoretical capacity and oxidation resistance than metastable VO_2(B) given the higher mean V valence (4.67) over VO_2(B).[24,25] Instead of bonding to one of the oxygen atoms in the VO_6 octahedron, the H_2O attaches to the vanadium and creates hydrogen bonds with the octahedron in the following layer.[26,27] Because of the mixed-valence of V^{4+}/V^{5+}, $H_2V_3O_8$ has a greater electrical conductivity than V_2O_5.[28,29] However, their electrochemical properties were affected due to poor electrical conductivity of the $H_2V_3O_8$ ARLBs. Researchers took effort to solve the problem, such as addition of graphene oxide. For example, Kang *et al.* used reduced graphene oxide composites to develop effective cathode materials in aqueous zinc-ion batteries and obtained high capacity, cycle stability, and electrochemical kinetics.[30] Wang *et al.* added took advantage of good electrical conductivity of one-dimension carbon nanotubes to construct flexible electrodes, which ensured fast electronic and ionic transport.[31]

In this study, $H_2V_3O_8$ nanorods doped with graphene (HVO/G) were well prepare using a simple hydrothermal process and following calcination. The HVO/G composites were calcined at an elevated temperature of 523 K to achieve improved performance. The HVO/G composite have been employed as the anode material for ARLBs, as shown in Fig. 1, which proved to be a very low-cost storage system with an aqueous saturated $LiNO_3$ solution. For comparison, $H_2V_3O_8$ nanorods (HVO) and $H_2V_3O_8$ nanorods doped with carbon nanotubes (HVO/CNTs) material were prepared similarly and calcined at the same temperature. The results show that the modified anode material can exhibit better electrochemical performances, including elevated specific discharge capacity of 271 mA h g^{-1} at 200 mA g^{-1}, a higher rate capacity of 125 mA h g^{-1} at 2 A g^{-1} without any decay of capacity after 60 cycles.

Experimental

Materials

The bulk V_2O_5 (purchased from Wako, Japan), graphene dispersion (5 mg mL^{-1}, water as the solvent, purchased from Zhitai, China), CNTs (purchased from Zhitai, China), acetone were directly used without any further purification.

Methods

HVO was made utilizing bulk V_2O_5 as the starting material in a single-step hydrothermal process. In a 50 mL beaker, 1.8 mmol of V_2O_5 was dissolved in 32 mL deionized water and 1 mL acetone in a conventional procedure. The mixture was evenly disseminated for 4 hours at room temperature using strong magnetic stirring. Then the above solution was transferred to a sealed autoclave at 453 K for 36 h. Using a centrifugal machine, the precipitate was repeatedly cleaned with deionized water and acetone. After 12 hours of drying at 353 K in a vacuum, a blue-green sheet-like product was formed. To optimize sintering temperature, as-synthesized materials were calcined in a series of temperatures (423 K, 473 K, 523 K, 573 K, respectively). To create $H_2V_3O_8$ nanorods with improved electrochemical performance, as-prepared materials were calcined in a tube furnace at an optimum temperature for 3 hours in flowing pure argon gas and cooled naturally.

HVO/G were synthesized by a similar hydrothermal method followed by calcination with 5.44 mL graphene dispersion added during the process.

HVO/CNTs were prepared in the same way as HVO/CNTs, except for 8 wt% CNTs added during the process.

The schematic preparation process is shown in Fig. 2.

Cell assembly

The HVO/G anode was utilized as the working electrode (WE), the saturated calomel electrode (0.242 *vs.* SHE/V) was used as the reference electrode (RE), and commercial $LiMn_2O_4$ was used as

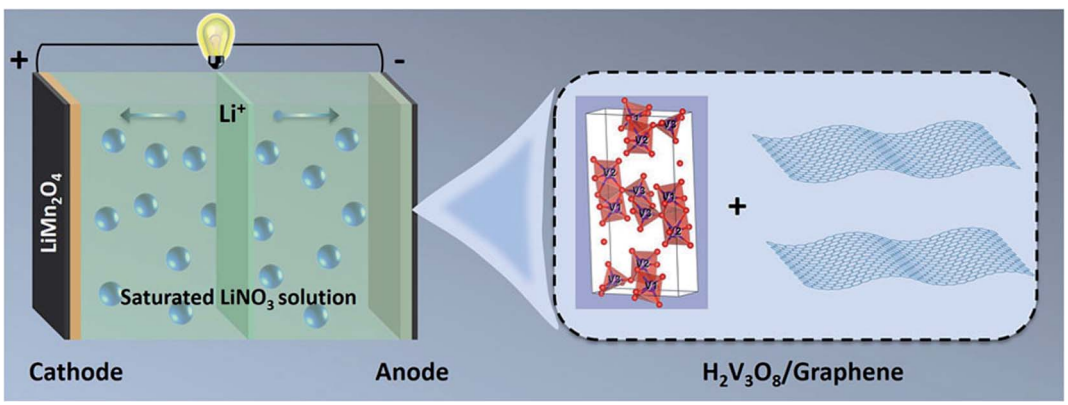

Fig. 1 The schematic diagram of ARLBs.

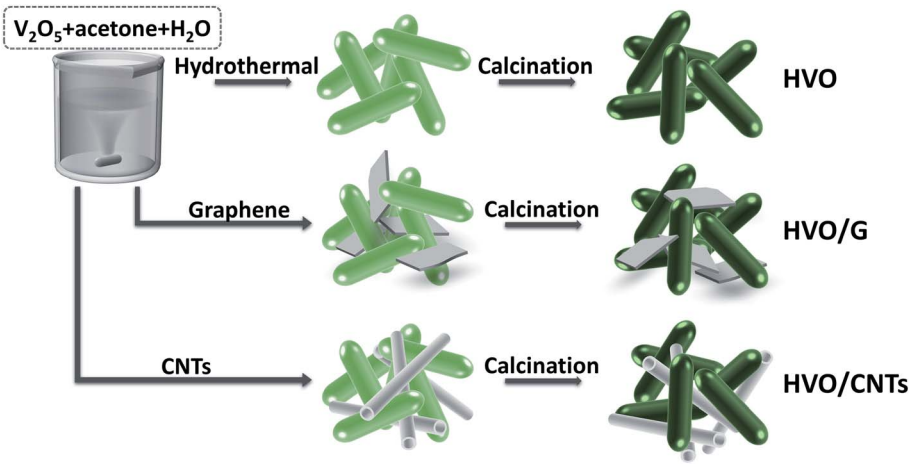

Fig. 2 The schematic preparation process.

the counter electrode in the three-electrode cell (CE). The WE was made by mixing active materials (HVO/G, 15 × 5 × 0.2 mm, 8 mg), acetylene black, and polyvinylidene fluoride (PVDF) in a weight ratio of 7 : 2 : 1. After utilizing *N*-methylpyrrolidone (NMP) as a solvent, the black slurry was uniformly mixed for about 2 minutes using an ultrasonic technique. To obtain the WE, the well-mixed anode material was coated on nickel mesh and dried at 373 K for 10 hours under vacuum. The CE was made with commercial $LiMn_2O_4$ by an identical process, whose amount was enough relative to the amount of the WE. The electrolyte came from saturated $LiNO_3$ solution, and to keep the pH of the electrolyte solution at 7, a suitable quantity of saturated $LiOH \cdot H_2O$ solution was dropwise put into the electrolyte solution. Before electrochemical testing, high quality nitrogen was breathed into the electrolyte to obtain a deoxygenated electrolyte.

Characterization

The phase structure was characterized by XRD using a BrukerD8-Advanced diffractometer. The SEM images were investigated by JEOL JSM-7000F, and the TEM, HRTEM, and SAED images were observed by JEOL JEM-2100. An Arbin BT2000 instrument operated the galvanostatic charge–discharge and rate performance of the ARLBs. In the aqueous electrolyte, the CV curves of ARLBs within −0.8-1 V (*vs.* SCE) at 2 mV s^{-1} and the EIS within 0.01–100 Hz was done using Ametek VMC-4. The thermal degradation behaviors of the samples were measured using a simultaneous thermal analyzer (METTLER TOLEDO TGA/DSC3, China). The samples were heated from 20 to 800 °C at a scan speed of 10 K min^{-1} in N_2 atmosphere. X-ray photoelectron (XPS) spectra were recorded on a Shimadzu Axis Ultra spectrometer with Al K alpha = 1361 eV excitation source.

Results and discussion

To optimize sintering temperature, as-synthesized materials were calcined at different temperatures, respectively. Fig. 3a shows the XRD patterns of the as-synthesized HVO samples after heating at 423 K, 473 K, 523 K, and 573 K for 3 h under a pure Ar environment. In Fig. 3a, the XRD pattern of as-synthesized material without calcination shows excellent consistency with Joint Committee on Powder Diffraction Standards (JCPDS) Card, No. 85-2401. All the diffraction peaks of these three materials heating at 423 K, 473 K, 523 K for 3 h under a pure Ar environment have no shift, which can be indexed to an orthorhombic $V_3O_7 \cdot H_2O$ ($H_2V_3O_8$) phase with the lattice parameters of $a = 16.93$ Å, $b = 9.36$ Å, $c = 3.64$ Å, $\alpha = \beta = \gamma = 90°$. The diffraction peaks such as (200), (011), (520), and (811) in XRD patterns of materials after sintering show the exact location as that of as-synthesized materials. However, peaks in the XRD pattern of materials sintering in different temperatures possess different strengths. The strength characteristic peak (200) for the orthorhombic $V_3O_7 \cdot H_2O$ ($H_2V_3O_8$) phase increases particularly, as the increasing temperature in the range of 423 to 523 K. However, the higher sintering temperature does not mean better diffraction peaks in the XRD pattern. While calcining at 573 K, the characteristic peak (200) disappears and it shows a more complex XRD pattern which can be indexed to a mixture phase of V_3O_7 and V_4O_9. Meanwhile, the peaks such as (011), (811), shift to the left obviously in the XRD patterns. The results demonstrate that the sintering temperature should not exceed 523 K, and the material after heat treatment at 523 K shows prominent peaks, indicating more perfect crystal integrity than materials calcined at others temperatures.

The thermogravimetric analysis (TGA) was used to study the development of the as-synthesized materials as the temperature was increased. Fig. 3b shows that below 523 K, the curve shows a delayed weight loss of 1.4 percent, owing to water evaporation and a little amount of acetone absorption mostly on material's surface. A quick weight loss was detected, suggesting a significant shift in the chemical composition and structure of the material at 523 K once the molecular H_2O in the $V_3O_7 \cdot H_2O$ ($H_2V_3O_8$) structure vanishes. Furthermore, the weight loss between 523 K and 693 K is about 8%, which is a little more than the ideal 6.36% weight loss in the $V_3O_7 \cdot H_2O$ ($H_2V_3O_8$). The reason is probably attributed to the further release of oxygen

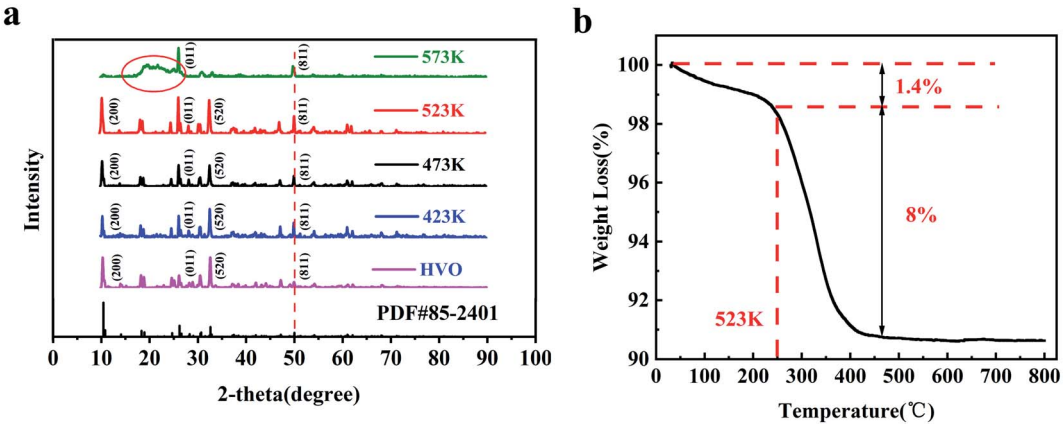

Fig. 3 (a) XRD of HVO samples without calcination and after heating at 423 K, 473 K, 523 K, 573 K. (b) TG curve of the HVO after vacuum drying at 353 K.

from the material, which is in accord with the presence of the V_4O_9 phase and V_3O_7 above 523 K.[20]

To discuss the effect of sintering temperatures on the morphology of HVO materials and determine the best sintering temperature for the electrochemical performance of ARLBs accurately, SEM images of HVO anode materials calcined at different temperatures and rate performance of ARLBs with different HVO anode materials are shown in Fig. 4a–d. Noticeable changes have occurred in the morphology and structure of HVO materials after being calcined at different temperatures. The length of HVO becomes shorter with the increase of sintering temperature, and the shorter nanorods interlink to form a more robust 3D network structure. But, the size of the material increases sharply after being calcined at 573 K. Furthermore, some small spherical particles impurities appear on the surface of nanorods, indicating the chemical composition and structure have changed in the matter of HVO above 523 K, which is consistent with previous XRD patterns and TG analysis.

The ARLBs with the electrode materials have been organized using a three-electrode cell immersed in saturated $LiNO_3$ aqueous electrolyte. The rate performance of ARLBs is shown in Fig. 4e. The ARLB with HVO calcined at 523 K exhibits the highest discharge capacity at every rate. The capacity retention of ARLBs with HVO calcined at 423 K, 473 K, and 523 K are all terrible when the rate comes back to 200 mA g^{-1}. The ARLB with $H_2V_3O_8$ nanorods calcined at 573 K releases the worst discharge capacity at every rate due to the most considerable nanorods size and chemical composition change. Smaller particles sizes and stronger 3D network structure are beneficial to create more pathways and shorten the transmission distance for lithium-ion, resulting in the ARLBs with HVO anode material calcined at 523 K possesses the best discharge capacity. Based on the above results, 523 K is the best sintering temperature for HVO anode material.

As to the method stated in the experimental section, HVO/G material was produced and subsequently calcined at 523 K for 3 hours. X-ray diffraction (XRD) was used to investigate the crystallography of the composite, as shown in Fig. 5. HVO/CNTs and HVO without doping were introduced at the same time for comparison. The presence of $H_2V_3O_8$ crystal structure in three

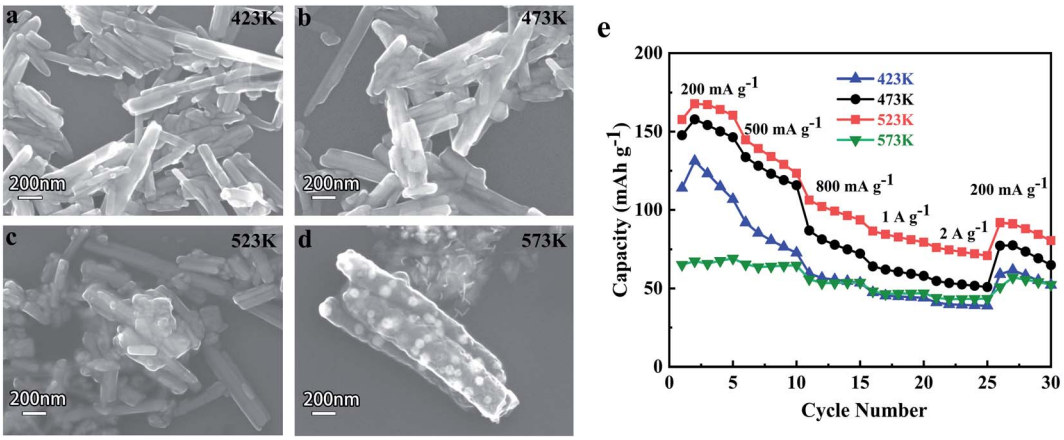

Fig. 4 SEM images of HVO anode materials and cycle performance of ARLBs. (a) SEM image of HVO calcined at 423 K. (b) SEM image of HVO calcined at 473 K. (c) SEM image of HVO calcined at 523 K. (d) SEM image of HVO calcined at 573 K. (e) Rate performance of ARLBs at 200 mA g^{-1}.

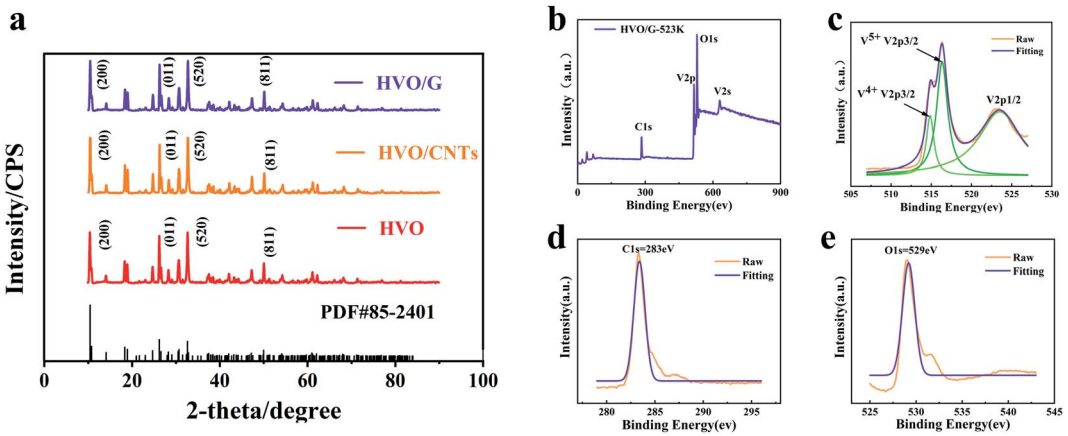

Fig. 5 (a) XRD patterns of HVO, HVO/CNTs and HVO/G. (b–e) XPS patterns of HVO/G.

composite materials is confirmed by characteristic peaks (200) in Fig. 5a. There is no visible difference given the distinct peaks in three XRD patterns which accurately match with the orthorhombic crystalline phase of $H_2V_3O_8$ (lattice parameters of $a = 16.93$ Å, $b = 9.36$ Å, $c = 3.64$ Å, $\alpha = \beta = \gamma = 90°$, space group: *Pnam*, JCPDS No. 85-2401). In addition, there are neither apparent peak shifts nor sharp peaks for graphene or CNTs in the patterns.

The valence state of HVO/G has been illustrated in Fig. 5b–e utilizing their respective XPS survey spectra. The peaks corresponding to V 2p, C 1s, and O 1s are clearly seen in Fig. 5b. By referring the C 1s to 283 eV, the binding energy found in the XPS investigation was rectified. Fig. 5c shows the V 2p core level spectrum, which shows two distinct peaks at 516 eV and 524 eV, which correspond to the V $2p_{3/2}$ and V $2p_{1/2}$ of V^{5+}, respectively. The lower-intensity signal centered at 516 eV verifies the existence of V^{4+} in a significant proportion. From the area of the peaks, the molar ratio of V^{4+}/V^{5+} is predicted to be 1 : 2.2, which is extremely near to the valence of V in $H_2V_3O_8$. The peak at 529 eV corresponding to O 1s binding energy in Fig. 5e demonstrates that the oxygen atoms exist as O^{2-} in the HVO/G materials.

The three-electrode materials' microstructure and morphology can be found in scanning electron microscope (SEM) images displayed in Fig. 6. HVO exhibit haphazard stack paths and identical nanorods with the size of 300–800 nm in lengths and 100–300 nm in diameters as shown in Fig. 6a. Obviously, the size of $H_2V_3O_8$ nanorods does not change in the lengths and diameters after adding CNTs, as shown in Fig. 6b. The most plausible reason is that CNTs whose structure is similar to nanowires could not influence the structure and microstructure of $H_2V_3O_8$ material. The SEM image of HVO/G is shown in Fig. 6c with an expected nanostructure and morphology. Within the randomly oriented nanorods, graphene sheets are thoroughly merged to produce a consistent micropores and 3D network nanostructure. Micropores in the electrode material are crucial to electronic capture, it helps to solve the volume impact during charging and discharging and facilitates fast mass transport.[32–37] Graphene sheets in the anode material can also give additional paths for lithium ions to pass through during charging and discharging.[38,39]

The detailed structure of HVO/G, HVO/CNTs, and HVO were further investigated by TEM in Fig. 7a–c and HRTEM (SAED inserted) in Fig. 7d–f. By comparing TEM and HRTEM images of three materials, the surface of all $H_2V_3O_8$ nanorods becomes rougher after calcination. Although a large number of CNTs can be observed in the microstructure in Fig. 7b, $H_2V_3O_8$ nanorods and CNTs are still in a state of separation. The morphology of $H_2V_3O_8$ nanorods does not change after adding CNTs in Fig. 7b, which is consistent with the results of SEM. In Fig. 7c, with the inclusion of graphene sheets, the $H_2V_3O_8$ nanorods may be connected to produce a 3D network

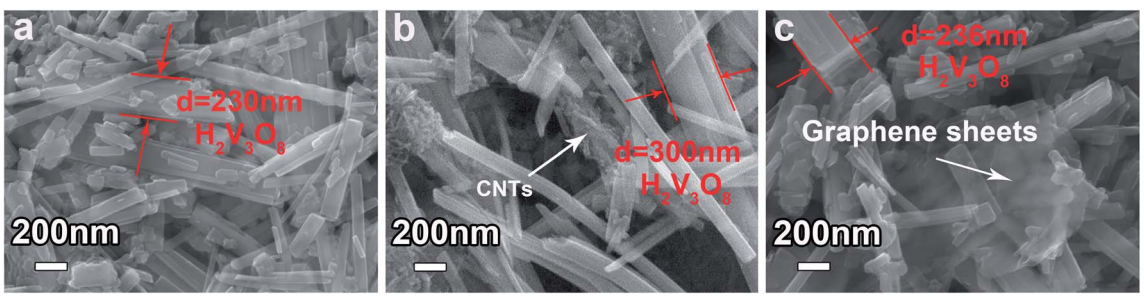

Fig. 6 (a) SEM images of HVO. (b) SEM images of HVO/CNTs. (c) SEM images of HVO/G.

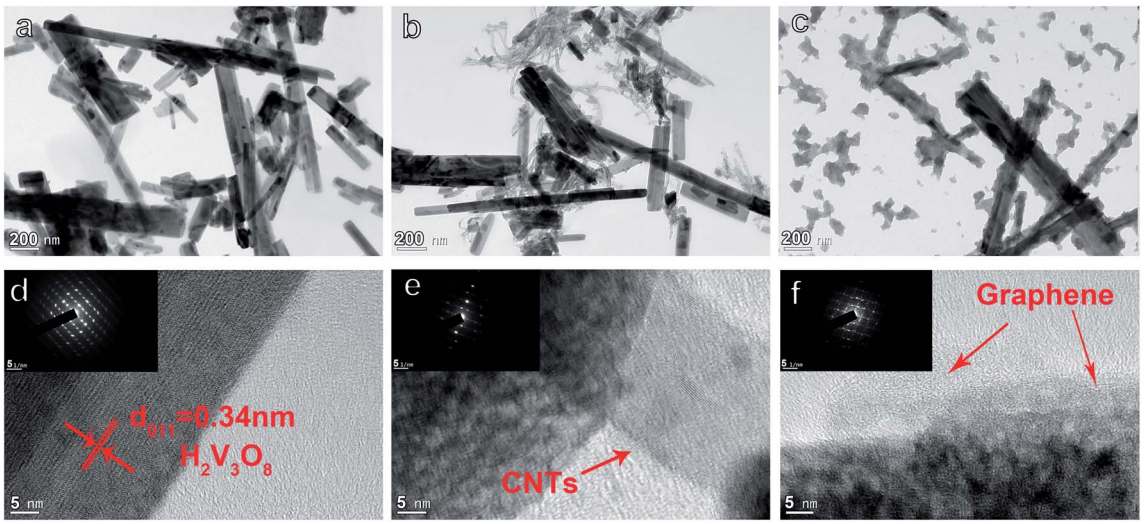

Fig. 7 (a–c) TEM images of HVO, HVO/CNTs and HVO/G. (d–f) HRTEM images (inserted images: SAED images) of HVO, HVO/CNTs and HVO/G.

nanostructure that matches SEM pictures. Graphene sheets work as binders to bring the scattered $H_2V_3O_8$ nanorods together, unlike pure $H_2V_3O_8$ nanorods, which disseminate independently and randomly.

The HRTEM image of HVO in Fig. 7d exhibits the high crystalline degree of $H_2V_3O_8$ nanorods with bright lattice fringes. The marked interplanar distance is 0.34 nm corresponding to the d_{011} spacing in the XRD patterns of $H_2V_3O_8$. Normal diffraction spots in inserted image in Fig. 7d also reveal that the material selected is monocrystalline. The surface of $H_2V_3O_8$ becomes rougher after adding CNTs in Fig. 7e, but the diffraction spots show no difference in the inserted image of Fig. 7d. The HRTEM image of HVO/G shows the tight link between nanorods, and graphene sheets is seen in Fig. 7f. Frequent diffraction spots and rounded shapes appear in an inserted image of Fig. 7f, meaning that HVO/G has both monocrystalline and polycrystalline nature. Therefore, we can indirectly detect the presence of graphene, showing that the supplement of graphene sheets alters the crystal structure of $H_2V_3O_8$ nanorods. The addition of graphene sheets to the surface of $H_2V_3O_8$ nanorods can significantly increase conductivity while the electrode material and the aqueous electrolyte infiltration resistance also lowered.

Fig. 8a–c shows the CV curves of ARLBs with HVO, HVO/CNTs and HVO/G, respectively. In Fig. 8, HVO, HVO/CNTs and HVO/G retain a CV curve with three pairs of redox peaks. In an organic electrolyte, this corresponds to three pairs of redox peaks for lithium intercalation and de-intercalation. Three pairs of peaks can be seen in the cathodic scan in the voltage ranges of 1.0 V and −0.8 V *vs.* SCE, as illustrated in Fig. 8b. The existence of lithium ions in distinct places throughout the insertion is demonstrated by an inconspicuous peak at 0.7 V, a wide peak centered at 0.1 V, and a narrow intense peak at −0.58 V. The three peaks correspond to the discharge reaction (as shown in eqn (1)), in which lithium ions embed into the $H_2V_3O_8$ structure from the electrolyte. Accordingly, it can be observed in the anodic scan that an inconspicuous peak is located at 0.82 V, a broad peak is centered at 0.25 V and a thin intensive peak is at −0.27 V, corresponding to a different charge reaction (as shown in eqn (2)), in which lithium ions escape from the $H_2V_3O_8$ structure into the electrolyte.

Discharging reaction:

$$H_2V_3O_8 + xLi^+ + xe^- \rightarrow Li_xH_2V_3O_8 \quad (1)$$

Charging reaction:

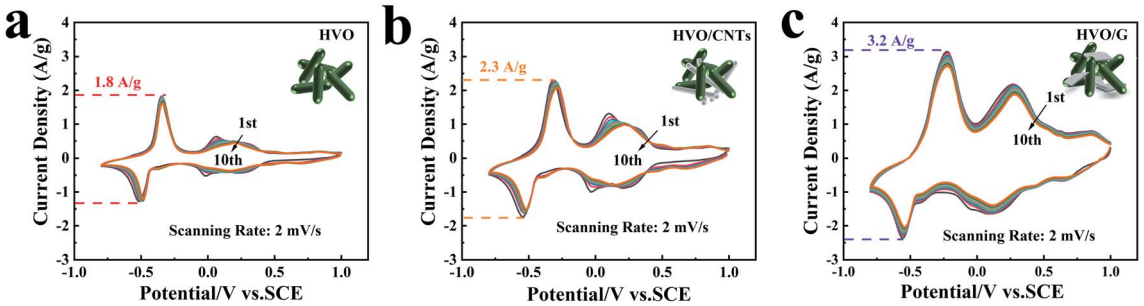

Fig. 8 CV curves. (a) Curves of 10 cycles of HVO. (b) Curves of 10 cycles of HVO/CNTs. (c) Curves of 10 cycles of HVO/G.

$$Li_xH_2V_3O_8 \rightarrow H_2V_3O_8 + xLi^+ + xe^- \quad (2)$$

Three CV curves in Fig. 8 are all excellent symmetry in shape, indicating that intercalation and de-intercalation of lithium ion in the $H_2V_3O_8$ structure are established theoretical and realistically. For aqueous rechargeable batteries, the principal side reaction of H_2 and O_2 evolution is critical. As shown in Fig. 8, there are no O_2 evolution peaks until the voltage rises to 1.0 V. There are no HER even when the voltage drops to −0.8 V, which means that the HER is poor in the $H_2V_3O_8$ electrode towards a further negative potential. The most significant difference between the curves in the three figures is that HVO/G possesses the most enormous current density corresponding to redox peaks, especially the peak centered at 0.1 V. Higher current density means higher charge and discharge capacity when charged and discharged. Furthermore, Fig. 8c demonstrates that after 10 cycles, the current density for a peak centered at 0.1 V exhibits low attenuation, indicating that the HVO/G electrode capacity may be adequately preserved when charged and discharged. As far as it can be seen, the network structure made by graphene sheets in HVO/G contributes to these good chemical properties.

The cycling performances and coulombic efficiency of (HVO/G)//(saturated $LiNO_3$)//$LiMn_2O_4$ ARLB, (HVO/CNTs)//(saturated $LiNO_3$)//$LiMn_2O_4$ ARLB, and HVO//(saturated $LiNO_3$)//$LiMn_2O_4$ ARLB at 200 mA g^{-1} current density are displayed in Fig. 9a. The ARLB with HVO/G anode material displays an improving cycling operation compared with HVO/CNTs and HVO electrodes. The first discharge capacity of ARLB with HVO/G is about 271 mA h g^{-1} and it still maintains 73.4% after 50 cycles (199 mA h g^{-1}). However, the first discharge capacity of ARLB with HVO/CNTs is somewhat lower (about 182 mA h g^{-1}) and then it increases to 208 mA h g^{-1}. However, the capacity quickly fades, and after 50 cycles, it only maintains 90 mA h g^{-1} with a 43 percent retention rate. The ARLB of HVO without doping had the worst cycling performance, with the lowest first discharge capacity (approximately 154 mA h g^{-1}), lowest peak capacity (about 189 mA h g^{-1}), and retention rate of 29%, demonstrating the relevance of graphene in aqueous rechargeable batteries' anode material. Therefore, adding graphene to anode materials in ARLBs can significantly increase cycling performance and initial discharge capacity. The doping of CNTs into the anode materials also can enhance the discharge capacity of ARLB, but it does not work to improve cycling performance. The ARLB with HVO/G anode has the best cycling performance and most stable coulombic efficiency (closest to 1) mainly on account of its low electrochemical resistance and particular 3D network structure made by graphene sheets, which can effectively avoid unexpected volume effect of the anode when charged and discharged.

The ARLBs' 3rd charge discharge curves in aqueous solution are shown in Fig. 9b. There are two evident plateaus and one inconspicuous plateau for HVO, HVO/CNTs and HVO/G electrodes, which indicate the redox reaction of $H_2V_3O_8$. The voltages of the three plateaus of three anodes are consistent with Fig. 8. The charge/discharge voltage plateau rises with the addition of graphene and CNTs, as demonstrated in Fig. 9b's curves. Still,

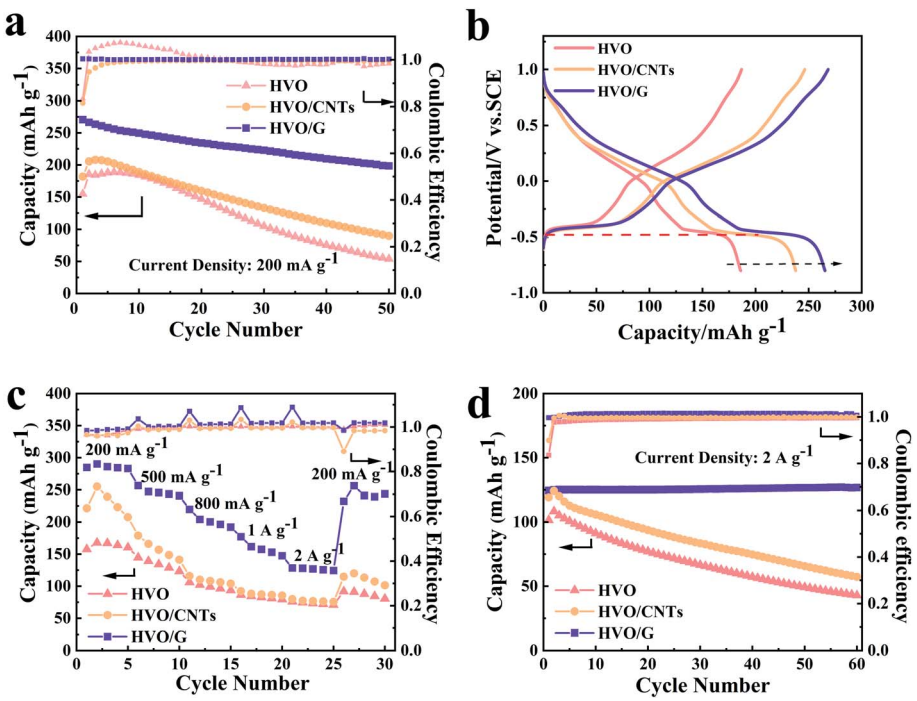

Fig. 9 (a) Cyclic performance and coulombic efficiency of ARLBs at 200 mA g^{-1}. (b) The 3rd charge–discharge curves of ARLBs. (c) Rate performance and coulombic efficiency of ARLBs with anode materials HVO, HVO/CNTs and HVO/G. (d) Cyclic performance and coulombic efficiency of ARLBs at 2 A g^{-1}.

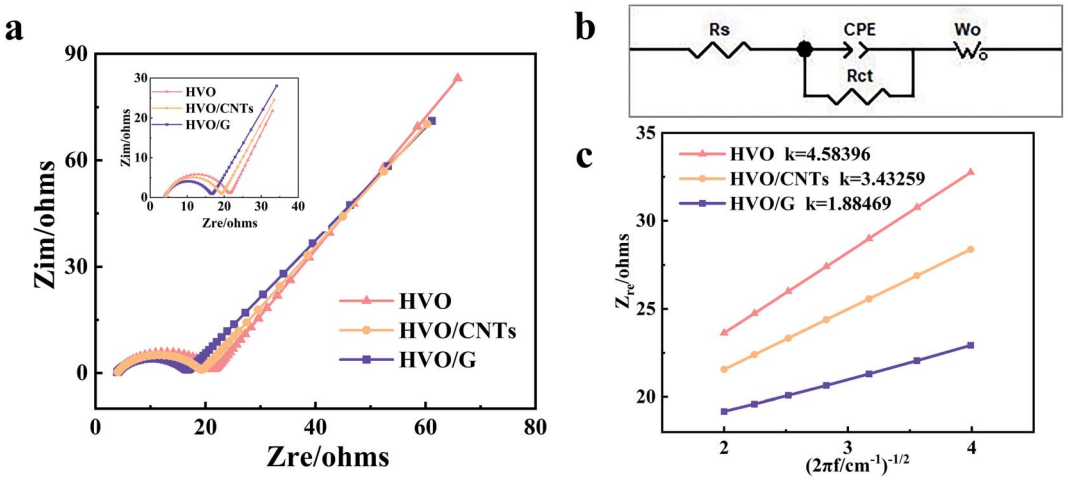

Fig. 10 (a) EIS testing yielded Nyquist plots of HVO/G, HVO/CNTs, and HVO (inset: an enlarged elevated-frequency area). (b) The corresponding circuit was employed to fit the data. (c) The fitting lines of the Z_{real}.

the potential difference among the charge and discharge voltage plateaus persists nearly unaltered, demonstrating that the addition of graphene or CNTs has minimal influence on the electrode materials' polarization and voltage lag.

The rate performance of ARLBs made of three different anode materials was examined under the same conditions in terms of CV and cycle performance, as shown in Fig. 9c. By gradually raising the current rate from 200 mA g^{-1} to 2 A g^{-1} and then abruptly reverting to 200 mA g^{-1}, the rate capability of three anode electrodes was assessed. The ARLB with HVO/G as anode electrode, is carried out at current rate from 200 mA g^{-1}, 500 mA g^{-1}, 800 mA g^{-1}, 1 A g^{-1} to 2 A g^{-1}, the capacities observed were 285 mA h g^{-1}, 257 mA h g^{-1}, 220 mA h g^{-1}, 177 mA h g^{-1} and 128 mA h g^{-1}, respectively. Then, when the ARLB is recycled at 200 mA g^{-1} for the last 5 cycles, the discharge capacity maintains at 256 mA h g^{-1} with retention of 89.8%, which is much higher than 51.6% of HVO/CNTs and 58.2% of HVO. Whatever the current rate is, the average discharge capacity of ARLB with HVO/G as anode electrode is higher than that of HVO and HVO/CNTs. Interestingly the electrochemical performance (discharge capacity and retention of capacity) of HVO/G has a more obvious superiority than that of $H_2V_3O_8$ nanorods when the current rate is back to 200 mA g^{-1}. HVO/CNTs anode material possesses a sophisticated preliminary discharge capacity but lower capacity retention than that of HVO anode material, meaning that the doping of CNTs can upsurge the preliminary discharge capacity but could not advance the cycling performance and rate performance of $H_2V_3O_8$ nanorods and material in ARLBs. The right *Y*-axis of Fig. 9c is responsible for the coulombic efficiency curves. The adown peaks in the coulombic efficiency curves illustrate the over discharge of ARLBs if the current density increases unexpectedly. There is an uncompleted discharge of ARLBs when the current density drops rapidly. Therefore, we can find by comparison in Fig. 9c that adding graphene to a system can increase cyclic stability, rate capability especially at higher current density, as well as retention rate of capacity as the current rate is back to low current density.

To examine the cycling performance of anode materials based on $H_2V_3O_8$ at superior current density, the cycling test at 2 A g^{-1} rate was organized in our experiment. In Fig. 9d, ARLB with HVO/G anode material exhibits an incredible cycling performance without decay of discharge capacity in such a huge current density. Meanwhile, the capacity curves of the other two ARLBs show a standard feature, in which the ARLBs are activated by high current density. Hence, the capacity increases obviously at the beginning of the testing. Although the ARLB with HVO/G experiences a high rate of 2 A g^{-1}, it can possess a sufficient capacity of 125 mA h g^{-1} without any decay of capacity after 60 cycles, which is better than that of the other two ARLBs. As shown on the right *Y*-axis of Fig. 9d, coulombic efficiency curves of three ARLBs have been presented. The ARLB with HVO/G coulombic efficiency is the steadiest. The enhancement of electrochemical performance at such a high current rate can be attributed to improved electrochemical kinetics of anode material, the capacitive effect from the high special area of graphene sheets, as well as weak volume effect caused by the special 3D network structure.

The EIS tests on HVO, HVO/CNTs and HVO/G anode electrodes in the ARLBs at a reduction state (−0.58 V) were conducted to look into the impact of lithium-ion diffusion characteristics onto materials electrochemical characteristics. The Nyquist plots, as shown in Fig. 10a, consist of a semicircle

Table 1 Electrochemical kinetics factors of HVO, HVO/CNTs and HVO/G

Material	R_s (Ω)	R_{ct} (Ω)	σ	D_{Li^+} (cm^2 s^{-1})
HVO	3.915	17.27	4.6	8.53×10^{-13}
HVO/CNTs	3.946	15.02	3.4	1.53×10^{-12}
HVO/G	3.839	12.55	1.9	4.89×10^{-12}

and an oblique line (inset is the enlarged graph within a high-frequency area). The charge transfer resistance (R_{ct}) among the aqueous electrolyte and the active material is shown by the semicircle, while the sloping line depicts the Warburg impedance generated by Li^+ diffusion in the electrode materials is represented by the slanting line.[28] The solution resistance of the electrolyte is explained by the junction between electrochemical impedance and the coordinate axis (R_s). Due to the presence of graphene, ARLB with HVO/G material shows lower R_{ct} and R_s value according to Table 1. Furthermore, equivalent circuit fitting has proved to be a standard method for analyzing electrochemical impedance in Fig. 10b. The constant-phase element (CPE) is the double-layer capacitance between the electrode material and the electrolyte. These simple electrical or electrochemical components in series or parallel roughly explain electrochemical kinetic processes. Eqn (3) and (4) may be used to compute D_{Li^+}:

$$D_{Li^+} = \frac{R^2T^2}{2A^2F^4n^4C^2\sigma^2} \quad (3)$$

$$Z_{real} = R_s + R_{ct} + \sigma\omega^{-1/2} \quad (4)$$

Here R represents gas constant, T represents temperature, A is the working electrode's surface area, n is the number of electrons per molecule in the redox process, F represents Faraday constant, and C is the Li^+ ion concentration in the electrode material, R is the gas constant, T is the absolute temperature, A is the working electrode's surface area, n is the number of electrons per molecule in the redox process, F stands for Faraday constant, and[17] the linear connection between Z_{real} and $\omega^{-1/2}$ may be used to calculate the slope (Fig. 10c). It's worth noting that the following eqn (5) may be used to calculate C:[40]

$$C = \frac{\rho}{M} \quad (5)$$

where ρ represents density as $\rho_{H_2V_3O_8} = 3.25\ g\ cm^{-3}$, and M is active materials molecular weight as $M_{H_2V_3O_8} = 282.84\ g\ mol^{-1}$. The matching diffusion coefficients of Li-ion are listed in Table 1, in which the D_{Li^+} value of HVO/G is $4.89 \times 10^{-12}\ cm^2\ s^{-1}$, three times higher than the D_{Li^+} values of HVO. The D_{Li^+} value of HVO/CNTs is still higher one order of magnitude than the D_{Li^+} value of $H_2V_3O_8$ nanorods. EIS data further implies that the adding of graphene can promote not only the ionic diffusion coefficient, but also the electrode reaction kinetics, which plays a positive role in electrochemical performance.

Table 2 provides the comparisons of discharge capacity, and the capacity retention among different working electrode materials and several electrolytes in a variety of battery systems, and our electrochemical capacities of HVO/G in this paper were also listed. As shown in Table 2, our HVO/G electrode material possesses competitive discharge capacity and good capacity retention and has the excellent electrochemical benefits at a higher rate. Therefore, our battery system has unique advantages, including simple assembly, low-cost material and equipment, pollution-free and a convenient testing environment.

Table 2 Electrochemical performance of several $H_2V_3O_8$ working electrodes in variety of battery systems

Working electrolyte materials	Electrolyte	Counter electrode	Battery system	Capacity in the 1st cycle	Capacity in the n^{th} cycle	Current density	Capacity retention
$H_2V_3O_8$/rGO[41]	1 M $LiPF_6$/EC + DMC	Li foil	LIB CR2032 coin-type cells	380/110	140(200^{th})/25(20^{th})	0.1 A g^{-1}/0.8 A g^{-1}	36.8%/22.7%
$V_3O_7 \cdot H_2O$/graphene[42]	1 M $LiPF_6$/EC + DMC	Si_3N_4/Li	LIB CR2032 coin-type cells	190	140(300^{th})	0.5 A g^{-1}	73.7%
$H_2V_3O_8$ nanowire[23]	5 M $LiNO_3$ + 0.001 M LiOH	Carbon	ARLB three-electrode battery	212	153(50^{th})	0.2 A g^{-1}	72%
$H_2V_3O_8$/rGO[43]	1 M $LiPF_6$/EC + DMC	Li foil	LIB CR2032 coin-type cells	100	117(50^{th})	1 A g^{-1}	117%
$H_2V_3O_8$ nanowire[24]	APC electrolyte	Mg metal	Magnesium-based battery CR2032	220/190	140(50^{th})/110(50^{th})	0.1 A g^{-1}/0.2 A g^{-1}	63.6%/57.9%
$H_2V_3O_8$ nanowire[44]	1 M $NaClO_4/C_4H_6O_3$	Na metal	Sodium-ion battery CR2016	70	50(280^{th})	0.1 A g^{-1}	71.4%
HVO/G[in this paper]	**Saturated $LiNO_3$**	**$LiMn_2O_4$**	**ARLB three-electrode battery**	**271/125**	**199(50^{th})/125(60^{th})**	**0.2 A g^{-1}/2 A g^{-1}**	**73%/100%**

Conclusions

A hybrid HVO/G was used as a potential anode for ARLBs. This composite was prepared *via* a simplistic one-step hydrothermal synthesis strategy and following calcination. After an optimized temperature of 523 K, a better electrochemical performance of HVO/G was obtained. HVO/CNTs and HVO materials were also prepared in the same condition to investigate the effect of the graphene in the $H_2V_3O_8$ nanorods material by comparing the microstructure of three-electrode materials and electrochemical performance of three ARLBs. The microstructure in the HVO/G composite with uniform $H_2V_3O_8$ nanorods and close contact among the $H_2V_3O_8$ graphene sheets and nanorods takes great advantages in rapid charge transfer kinetics, low electrochemical resistance, and weak volume impact than HVO/CNTs and HVO material. A new ARLB was fabricated with HVO/G anode and commercial $LiMn_2O_4$ cathode in the saturated $LiNO_3$ aqueous solution. Three pairs of redox peaks with good symmetry in CV curves of ARLB with HVO/G anode confirm the rapid and reversible Li^+ intercalation/extraction not including HER and OER side reactions. The ARLB with HVO/G can deliver an ideal specific capacity of 271 mA h g^{-1} and keep a retention rate of 73.4% after 50 cycles. At every current rate, ARLB with HVO/G as anode electrode performs better than that of HVO/CNTs and HVO as far as the average discharge capacity is concerned. Even at 2 A g^{-1} current density rate, it can possess a surprising capacity of 125 mA h g^{-1} without any decay of capacity after 60 cycles, which is more outstanding than that of the other two ARLBs. The addition of graphene offers a high diffusion coefficient of lithium-ion, which is increased by one order of magnitude than that of the other compared anode materials. The electrochemical increase is due to a capacitive effect caused by the large particular area of graphene sheets, better kinetics of the anode material, and a unique 3D network topology. The new ARLB with HVO/G electrodes provides a promising energy storage system with significant advantages, including low-cost preparation, easy assembly process, environmental protection and excellent safety.

Conflicts of interest

There are no conflicts to declare.

Acknowledgements

The National Natural Science Foundation of China (No. 52173263), the Natural Science Foundation of Anhui Province, China (No. 2108085J11), the Regional Innovation Capability Guidance Program of Shaanxi (No. 2022QFY03-02), the Northwestern Polytechnical University's Fundamental Research Funds for Central Universities (No. D5000210825), Natural Science Basic Research Plan in Shaanxi Province of China (No. 2022JQ-533), and Scientific research fund for high-level talents of Xijing University (No. XJ21B18) all contributed to this research. We would also like to thank the Xi'an Key Laboratory of Advanced Photo-electronics Materials and Energy Conversion Device for their Support (Xijing University).

Notes and references

1 N. Nitta, F. X. Wu, J. T. Lee and G. Yushin, *Mater. Today*, 2015, **18**, 252–264.
2 M. Hadouchi, T. Koketsu, Z. Hu and J. Ma, *Battery Energy*, 2022, **1**, 20210010.
3 J. Liu, J. P. Hu, Q. Deng, J. Mo, H. Xie, Z. C. Liu, Y. F. Xiong, X. W. Wu and Y. P. Wu, *Isr. J. Chem.*, 2015, **55**, 521–536.
4 C. J. Lei, F. F. Wang, J. Yang, X. F. Gao, X. Y. Yu, B. Yang, G. H. Chen, C. Yuan, L. C. Lei and Y. Hou, *Ind. Eng. Chem. Res.*, 2018, **57**, 13019–13025.
5 H. Zhang, L. Wang and X. He, *Battery Energy*, 2022, **1**, 20210011.
6 Y. J. Li, X. Hou, Y. Zhou, W. Q. Han, C. Liang, X. Wu, S. F. Wang and Q. Ru, *Energy Technol.*, 2018, **6**, 391–396.
7 D. Kornilov, T. R. Penki, A. Cheglakov and D. Aurbach, *Battery Energy*, 2022, **1**, 20210002.
8 Y. Wang, J. Yi and Y. Xia, *Adv. Energy Mater.*, 2012, **2**, 830–840.
9 B. B. Kopuklu, A. Tasdemir, S. A. Gursel and A. Yurum, *Carbon*, 2021, **174**, 158–172.
10 J. Liu, C. Xu, Z. Chen, S. Ni and Z. X. Shen, *Green Energy Environ.*, 2018, **3**, 20–41.
11 G. Pang, P. Nie, C. Z. Yuan, L. F. Shen, X. G. Zhang, J. J. Zhu and B. Ding, *Energy Technol.*, 2014, **2**, 705–712.
12 Z. Yan, Z. Sun, A. Li, H. Liu, Z. Guo and L. Qian, *Adv. Compos. Hybrid Mater.*, 2021, **4**, 716–724.
13 W. Li, J. R. Dahn and D. S. Wainwright, *Science*, 1994, **264**, 1115–1118.
14 Y. Wang, S.-Z. Yang, Y. You, Z. Feng, W. Zhu, V. Gariepy, J. Xia, B. Commarieu, A. Darwiche, A. Guerfi and K. Zaghib, *ACS Appl. Mater. Interfaces*, 2018, **10**, 7061–7068.
15 X. J. Wang, Y. Y. Hou, Y. S. Zhu, Y. P. Wu and R. Holze, *Sci. Rep.*, 2013, **3**, 5.
16 A. Caballero, J. Morales and O. A. Vargas, *J. Power Sources*, 2010, **195**, 4318–4321.
17 M. S. Zhao, W. G. Zhang and X. P. Song, *Dalton Trans.*, 2017, **46**, 3857–3863.
18 A. Yuan, T. Lei, W. Xu and Y. Wang, *J. Power Sources*, 2010, **195**, 5032–5038.
19 W. Pei, Y. Hui and H. Yang, *J. Power Sources*, 1996, **63**, 275–278.
20 Q. Pang, C. L. Sun, Y. H. Yu, K. N. Zhao, Z. Y. Zhang, P. M. Voyles, G. Chen, Y. J. Wei and X. D. Wang, *Adv. Energy Mater.*, 2018, **8**, 9.
21 N. Zhang, Y. Dong, M. Jia, X. Bian, Y. Wang, M. Qiu, J. Xu, Y. Liu, L. Jiao and F. Cheng, *ACS Energy Lett.*, 2018, **3**, 1366–1372.
22 H. Qiao, X. Zhu, Z. Zheng, L. Liu and L. Zhang, *Electrochem. Commun.*, 2006, **8**, 21–26.
23 H. Li, T. Zhai, P. He, Y. Wang, E. Hosono and H. Zhou, *J. Mater. Chem.*, 2011, **21**, 1780–1787.
24 H. Tang, N. Xu, C. Pei, F. Xiong, S. Tan, W. Luo, Q. An and L. Mai, *ACS Appl. Mater. Interfaces*, 2017, **9**, 28667–28673.
25 H. L. Chen, S. L. Cheng, D. Chen, Y. Jiang, E. H. Ang, W. L. Liu, Y. Z. Feng, X. H. Rui and Y. Yu, *Mater. Chem. Front.*, 2021, **5**, 1585–1609.

26 P. He, Y. Quan, X. Xu, M. Yan, W. Yang, Q. An, L. He and L. Mai, *Small*, 2017, **13**, 1702551.
27 Y. Ma, M. Wu, X. Jin, R. Shu, C. Hu, T. Xu, J. Li, X. Meng and X. Cao, *Chem.–Eur. J.*, 2021, **27**, 12341–12351.
28 S. Sarkar, A. Bhowmik, J. Pan, M. D. Bharadwaj and S. Mitra, *J. Power Sources*, 2016, **329**, 179–189.
29 Y. Zhou, Q. Pan, J. Zhang, C. Han, L. Wang and H. Xu, *Adv. Sci.*, 2021, **8**, 2002579.
30 J.-S. Park, S. E. Wang, D. S. Jung, J.-K. Lee and Y. C. Kang, *Chem. Eng. J.*, 2022, **446**, 137266.
31 X. Wang, Y. Wang, J. Hao, Y. Liu, H. Xiao, Y. Ma, L. Chen, Y. Huang and G. Yuan, *Energy Storage Mater.*, 2022, **50**, 454–463.
32 W. Alkarmo, F. Ouhib, A. Aqil, J. M. Thomassin, B. Vertruyen, M. L. Piedboeuf, N. Job, C. Detrembleur and C. Jerome, *J. Mater. Sci.*, 2018, **53**, 6135–6146.
33 Y. L. Xing, B. Z. Fang, A. Bonakdarpour, S. C. Zhang and D. P. Wilkinson, *Int. J. Hydrogen Energy*, 2014, **39**, 7859–7867.
34 B. Z. Fang, J. H. Kim and J. S. Yu, *Electrochem. Commun.*, 2008, **10**, 659–662.
35 B. Z. Fang, L. Daniel, A. Bonakdarpour, R. Govindarajan, J. Sharman and D. P. Wilkinson, *Small*, 2021, **17**, 2102288.
36 Y. Lu, Y. Wang, C. Xu, C. Xie, W. Li, J. Ding, W. Zhou, Z. Qin, X. Shen and L. B. Luo, *Nanoscale*, 2021, **13**, 3709–3722.
37 B. Z. Fang, J. H. Kim, M. S. Kim and J. S. Yu, *Acc. Chem. Res.*, 2013, **46**, 1397–1406.
38 Z. L. Zhang, Y. H. Wang, D. Li, Q. Q. Tan, Y. F. Chen, Z. Y. Zhong and F. B. Su, *Ind. Eng. Chem. Res.*, 2013, **52**, 14906–14912.
39 M. Zhong, J. Yan, H. Wu, W. Shen, J. Zhang, C. Yu, L. Li, Q. Hao, F. Gao, Y. Tian, Y. Huang and S. Guo, *Fuel Process. Technol.*, 2020, **198**, 106241–106248.
40 X. Y. Wang, H. Hao, J. L. Liu, T. Huang and A. S. Yu, *Electrochim. Acta*, 2011, **56**, 4065–4069.
41 Z. W. Liu, R. X. Xu, W. Wei, P. Jing, X. Li, Q. Y. Zhu, H. J. Sun, Y. Y. Dong and G. S. Zakharova, *Solid State Ionics*, 2019, **329**, 74–81.
42 Z. Y. Tian, N. Li, K. Xie and C. M. Niu, *J. Power Sources*, 2019, **417**, 14–20.
43 K. Zhu, X. Yan, Y. Zhang, Y. Wang, A. Su, X. Bie, D. Zhang, F. Du, C. Wang, G. Chen and Y. Wei, *Chempluschem*, 2014, **79**, 447–453.
44 D. Wang, Q. Wei, J. Sheng, P. Hu, M. Yan, R. Sun, X. Xu, Q. An and L. Mai, *Phys. Chem. Chem. Phys.*, 2016, **18**, 12074–12079.